# Uncovering the white etching area and crack formation mechanism in bearing steel

Ksenija Nikolic [a,b], Vitoria Mattos Ferreira [c] , Loïc Malet [d] ,Tom Depover [e], Kim Verbeken [e], Roumen H. Petrov [a,c]

[a] *Ghent University, Department Electromechanical, Systems & Metal Engineering, Technologiepark 46, 9052 Ghent, Belgium*

[b] *SIM vzw, Technologiepark 48, 9052 Zwijnaarde, Belgium*

[c] *Delft University of Technology, Department of Materials Science and Engineering, Mekelweg 2, 2600, The Netherlands*

[d] *Ecole Polytechnique de Bruxelles, Campus du Solbosch, Avenue F.D. Roosevelt 50, 1050 Bruxelles*

[e] *Ghent University, Department Materials, Textiles and Chemical Engineering, Technologiepark 46, 9052 Ghent, Belgium*

ABSTRACT

The microstructure of a damaged bearing from the field was characterized in this work with the intention to better understand microstructural features behind formation of White Etching Cracks (WEC) in bearings. Microstructural characterization of the altered white etching area (WEA) involved conventional electron backscattered diffraction (EBSD), followed by transmission electron microscopy (TEM), and transmission Kikuchi diffraction (TKD). In addition, automated crystallographic orientation mapping in TEM was performed on lamellae from selected regions of the WEA extracted via focus ion beam milling. The results revealed that the orientation of detectable grains within WEA is similar to that of the vicinal bulk material. WEA consists of small spherical grains (average 30 nm) and the orientation of the grains varied significantly in the deformed zone, suggesting that recrystallization had occurred. The interface between bulk material and the deformed zone is very sharp. Furthermore, needle-like grains, most likely originating from the zone undergoing only modest levels of severe plastic deformation, occurred in WEA. The occurrence of different grain sizes in WEA and incomplete plastic deformation strongly support the hypothesis of WEC formation via severe plastic deformation followed by recrystallization.

*Keywords*: Rolling Contact Fatigue, White Etching Cracks, White Etching Area, Bearing steel, EBSD, FIB, TEM,

Corresponding author: Ksenija Nikolic, telephone number +32 468 04 01 91
Technologiepark 46, 9052, Belgium
*Email address*: Ksenija.nikolic@ugent.be

## 1. Introduction

The European Commission's strategy for 2050 explicitly calls for a substantive increase in installed renewable energy capacity and a reduction in the emissions of greenhouse gases [1]. Various studies have acknowledged wind energy as a critical enabler for achieving 100% renewable energy penetration [2, 3]. Offshore wind energy is considered an important source of renewable energy and has experienced rapid growth in recent years, especially in north-western European countries [4]. One of the limitations in achieving these goals is the operation and maintenance cost, particularly in the case of offshore wind farms [5]. In the windmills, the high and sometimes unpredictable failure rate of the gearboxes, which are structural components, increases the costs and downtime [6]. The predicted lifetime of wind turbine gearboxes is 20 years. However, the actual lifespan is often shorter than this desired lifespan. The damage in the bearings in the gearboxes is frequently associated with the formation of white etching cracks (WECs). WECs are subsurface cracks often formed around non-metallic inclusions located in the region of the highest Hertzian stresses. The term WECs refers to the white appearance of the cracks after metallographic sample preparation and etching; the cracks are resistant to most common metallographic etchants containing 2 to 4vol % nitric or/picric acid in ethanol (i.e., Nital and Picral). Furthermore, WECs are mainly initiated around non-metallic inclusions that act as high-stress concentrators [7]. The initial stage of damage leads to the formation of "butterfly wing" (BW), where the damage propagates most commonly from non-metallic inclusions at an angle of 30° with respect to the rolling direction. During the rolling contact cycles, the BWs/WECs develop crack networks, and upon reaching the surface, lead to spalling of the raceway surface. Consequently, the microstructural features around WECs are altered and consist of nanocrystalline ferrite. This region is referred to as the white etching area (WEA). Despite extensive research on WEA formation, a generally accepted damage mechanism has yet to be identified. Many mechanisms have been proposed in the literature, but debates regarding the chronology of WEC and WEA appearance persist.
In the literature, many engineering factors have been identified as potential initiators for WEC formation. Misalignment of the bearing, loads, lubrication, slip, and electrical currents are considered the main surface initiators of WECs [8, 9, 10, 11, 12]. In addition, the subsurface

mechanism is attributed mainly to inclusions, residual stresses, microstructural defects, and secondary phases [13]. A thorough literature review of the different mechanisms responsible for WEC is provided by Warhadpande et al. [14] and Sadeghi et al. [15].

Through-hardened bearings are most often fabricated from a steel alloy referred to as 52100 steel, which consists mainly of ~1%C and ~1.5%Cr (mass%). After the final thermal treatment, which includes oil quenching and low-temperature tempering (~160°C), the steel microstructure consists of ~4% spherical secondary cementite type (θ) carbides formed during spheroidization annealing. These carbides are embedded in a matrix of tempered martensite, retained austenite, and one or more of the η, ε carbides [16]. After low-temperature tempering, the martensite strength is determined by the carbon in solid solution, high dislocation density, small grain size, and fine transition carbides, predominantly ε-carbide [17]. However, the microstructure of the WEA formed around the crack differs significantly from the one described above. Several works [18, 19, 20, 21] have reported that the WEA consists of nanocrystalline body-centered cubic (BCC) ferrite (grain size: 10 nm–300 nm), and chromium-rich cementite type carbides are absent from the WEA [18, 19, 22, 23]. Moreover, according to previous studies [24, 25], the WEA is 30–50% harder than the undamaged zone, and is separated from this zone by a sharp interface. Using wave dispersive X-ray spectroscopy (WDS), Curd et al. [26] determined the carbon content in the vicinity of the WEA and further away in the undamaged zone. The carbon content of the zone near WEA was the same as that of the bulk material. This result countered the hypothesis that the formation process of WEA consumed carbides in the vicinity of WEA, thereby preventing further development of WEA. Other authors observed inhomogeneous regions with coarse and needle-like grains within regions with fine grains or in the matrix/WEA boundary region [27]. When the material was prepared via focused ion beam (FIB) milling, these grains also appeared needle-shaped, suggesting that such grains are characterized by a three-dimensional (3D) plate-like morphology. Moreover, the long needle-shaped grains had low Kernel Average Misorientation (KAM) values in groups with similar orientations and preferred growing directions. These grains often appeared with a sharp boundary in zones with the finest grain sizes, suggesting that they formed due to secondary transformation induced by thermal annealing. Li et al. [18] further investigated the WEA using atom probe tomography (APT). The findings revealed that the grains in the WEA were equiaxed and the grain boundaries were decorated with carbon

and were uniformly distributed throughout the entire volume. These results support the hypothesis that supersaturated carbon-enriched nano-sized ferrite is formed in the WEA.

Many different mechanisms have been proposed as possible reasons for WEA formation. Some of the proposed mechanisms are: *(i)* severe plastic deformation (SPD) [18, 28], *(ii)* carbide dissolution [18], *(iii)* low-temperature recrystallization [22], and *(iv)* dislocation-assisted carbon migration [29]. Although WEA formation has been extensively investigated, a universal explanation of the WEA phenomenon is lacking. The chronological appearance of alterations, i.e., WEC/WEA, remains unclear. Some authors claim that the formation of WEC precedes the formation of WEA [28], while others suggest that first, WEA forms and cracks propagate due to the harder microstructure (compared with the microstructure preceding WEA formation) [26, 30]. To clarify (at least partially) the abovementioned issues, the altered area of a field bearing is systematically characterized in the present study.

## 2. Material and methods

A through-hardened bearing steel with chemical composition corresponding to AISI 52100 steel grade (see Table 1) was investigated in this work. The microstructure consists of tempered martensite and spherical carbides of type $M_3C$, where M is Fe and/or Cr. The bearing was collected from the field after unknown hours of operation when axial cracking occurred. The bearing was cut to reveal the axial plane (see Figure 1) and prepared for metallographic observations. The specimens were gently sectioned using a silicon carbide cutting disc on a Struers Discotom-5 cutting machine. To prepare the surface for analysis, the standard metallographic approach employing a series of progressively finer grinding papers, from P180 to P2000, was used. Grinding was followed by a series of polishing steps, using 3 µm and 1 µm diamond polishing solution. Samples were then etched using Nital 2% (2vol% $HNO_3$ solution in $C_2H_5OH$) to reveal the microstructure for observation via light optical microscopy and scanning electron microscopy (SEM). To prepare the sample surface for electron backscatter diffraction (EBSD) measurements, the samples were polished for an additional 10 min with colloidal silica (OPS) with an abrasive particle size of 35 nm.

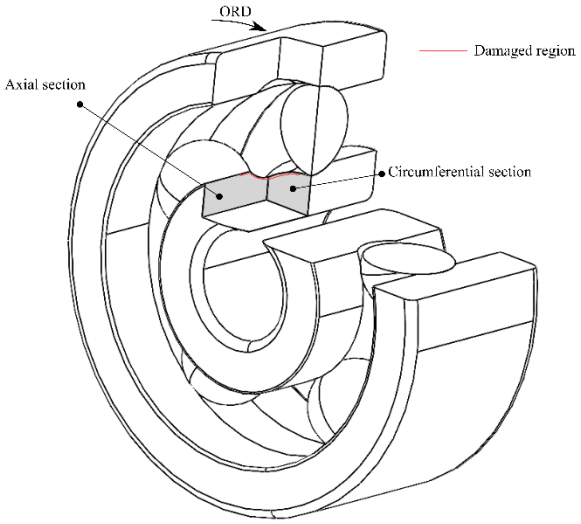


*Figure 1. Schematic showing the axial and circumferential sections of a bearing*

SEM images were acquired on a FEI Quanta 450-FEG-SEM (FEI Company, Hillsboro, OR, USA) operating at 15kV. A final beam aperture of 50 µm and a spot size of 5, which corresponds to a probe current of 2.3 nA in secondary electron (SE) and backscatter electron (BSE) imaging mode, were employed. The angular accuracy of the system is ~0.5°. The same microscope was used for EBSD. Data acquisition was performed under the following conditions: accelerating voltage of 15 kV, beam current of ~2.3 nA, corresponding to a FEI spot size of 5, and working distance of 12 mm. The resulting patterns were acquired on a hexagonal scan grid using a Hikari detector operated with EDAX TSL-OIM Data Collection version 6 software (AMETEK materials analysis division, Mahwah, NJ, USA). The EBSD scans were performed at a step size of 30 nm. The corresponding orientation data were post-processed with EDAX-TSL-OIM data analysis software version 7.3 using the following grain definition: misorientation with neighboring grains: higher than 5°, the minimum number of points per grain: seven, and confidence index (CI): higher than 0.2. The grain size in this work was taken as the calculated average grain diameter, i.e., the diameter corresponds to a grain of the same area, consisting of the points that fulfill the above conditions. The raw EBSD data were post-processed and dubiously indexed points were reassigned by applying the grain CI standardization and neighbor CI correlation procedure in a single step. Applying this procedure changed no more than 5% of the original data. To derive the grain size within the WEA, only grain boundaries with misorientation angles larger than 5° and grains larger than 3 pixels were considered.

The transmission electron microscopy (TEM) samples are prepared via Thermo Fisher's Helios G4 UXe by Focus Ion Beam (FIB) milling. To preserve the surface characteristics during FIB milling, a rectangular protection layer (platinum) is first deposited on the top of the region of interest. Milling is then performed on the surroundings of the region protected by the platinum layer. This leads to the formation of a lamella (TEM sample), which is then lifted out from the specimen and welded to a copper holder. Subsequently, a lamella-thinning process is performed by means of repeated FIB milling with decreasing current and/or voltage. The final lamella thickness should be approximately 10–100 nm for TEM analysis.

Automated Crystal Orientation Mapping (ACOM TEM) measurements (step size: 8 nm) are performed on a Philips CM20 microscope operated at 200kV using the ASTAR® system [31].

*Table 1. Chemical composition of through-hardened bearing steel investigated in this work*

| *Element* | *C* | *Mn* | *P* | *S* | *Si* | *Cr* | *Cu* | *Mo* | *Ni* |
|---|---|---|---|---|---|---|---|---|---|
| *Wt.%* | 0.96 | 0.27 | 0.02 | 0.01 | 0.25 | 1.6 | 0.2 | 0.15 | 0.18 |

## 3. Results

### *3.1 Microstructural characterization of the damage formation in the field bearing*

The field bearing analyzed in this work failed prematurely via axial cracking. Therefore, the study focused on determining whether the observed damage is associated with the WEC phenomenon. Local damage in the shape of BWs around non-metallic inclusions and WECs occurs within the subsurface of the bearing. BWs without branching or networks are located close (within ~100 µm) to the raceway surface. However, the crack networks (WECs) are only present at 300 µm from the surface, which coincides with the zone of maximum Hertzian stresses. The BWs may be located very close (~30 µm) to, but never reach, the raceway surface. Most of the observed WECs/WEAs are already connected to crack networks, suggesting that they are in the late stage of damage evolution. However, with the observation of two-dimensional (2D) cross-sections, 3D objects appear as 2D objects (lines) or points. Hence, in this work, we focus on the WECs, which are both short and separate (rather than connected in networks), in order to capture the intermediate stage of WEC development. Figure 2 shows a SEM image of a crack surrounded by WEA. The crack starts from a non-metallic inclusion and has an irregular shape with a bump-like region of WEA developed above

the crack. In the same zone, the WEC is located close to the bottom of the altered region, as indicated by the red square in Figure 2a. The secondary electron image presented in Figure 2b shows a magnified view of an irregular bump-like region of WEA. Chromium carbides are absent from this zone, but are vicinal to the deformed zone.

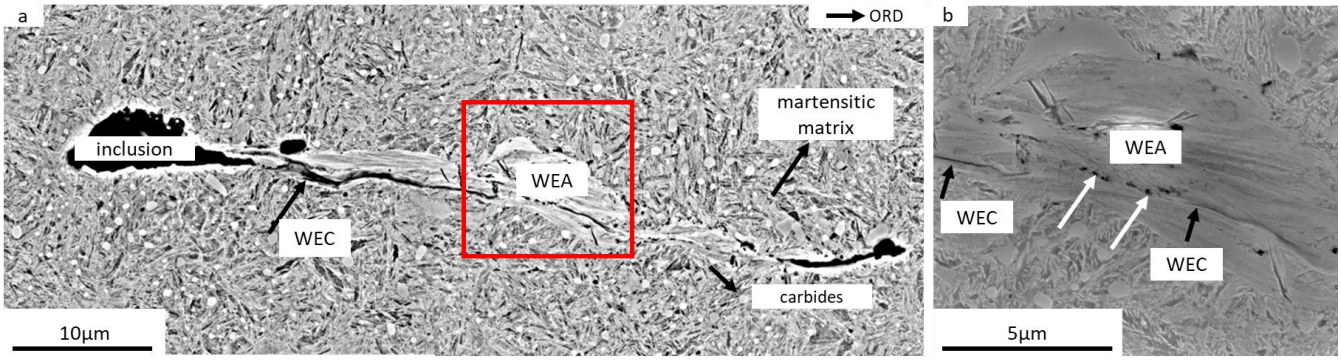


*Figure 2. (a) BSE image of a region with WEC originating from non-metallic inclusions. Over-rolling direction (ORD) is indicated by the black arrow. The region enclosed in the red square is shown in Figure 2 (b). (b) Magnified view of WEA shown in (a) and vicinal bulk material. WECs are located in the lower part of WEA, and the growth of these carbides seems slightly interrupted. A few voids are formed between the two parts of non-connected WECs, as indicated by white arrows. Chromium carbides are vicinal to, but absent from, the WEA.*

The same zone is characterized by EBSD, which revealed the presence of grains with martensite-like morphology inside WEA (Figure 3a); the analysis was performed on the regions enclosed in the white rectangles shown in Figure 3a. The WEA and WEC are distinguished by including points with CI below 0.2 in the image quality (IQ) map. If the CI<0.2 points are excluded from the EBSD map, this zone would have appeared dark in the image and, therefore, WEA and WEC would be indistinguishable. However, the CI of each point in the inverse pole figure (IPF) map is larger than 0.2. To gain additional information on the morphology and damage formation, KAM values are calculated using the average misorientation of a given pixel with its third neighbor (upper limit: 5°). The misorientation determined for resolvable grains within the WEA is similar to that of the grains in the bulk material. This suggests that no recrystallization has occurred (the expectation is that, after recrystallization, the misorientation between grains within WEA would be lower than the misorientation between the grains in the bulk) [27]. Two specific areas are selected for further analysis. The first area corresponds to the martensitic matrix and shows the smooth appearance of WEA (indicated by rectangle 1 shown in image Figure 3a). The second area corresponds to the matrix and contains a part of the WEA with relatively large grains (indicated by rectangle 2 in Figure 3a).

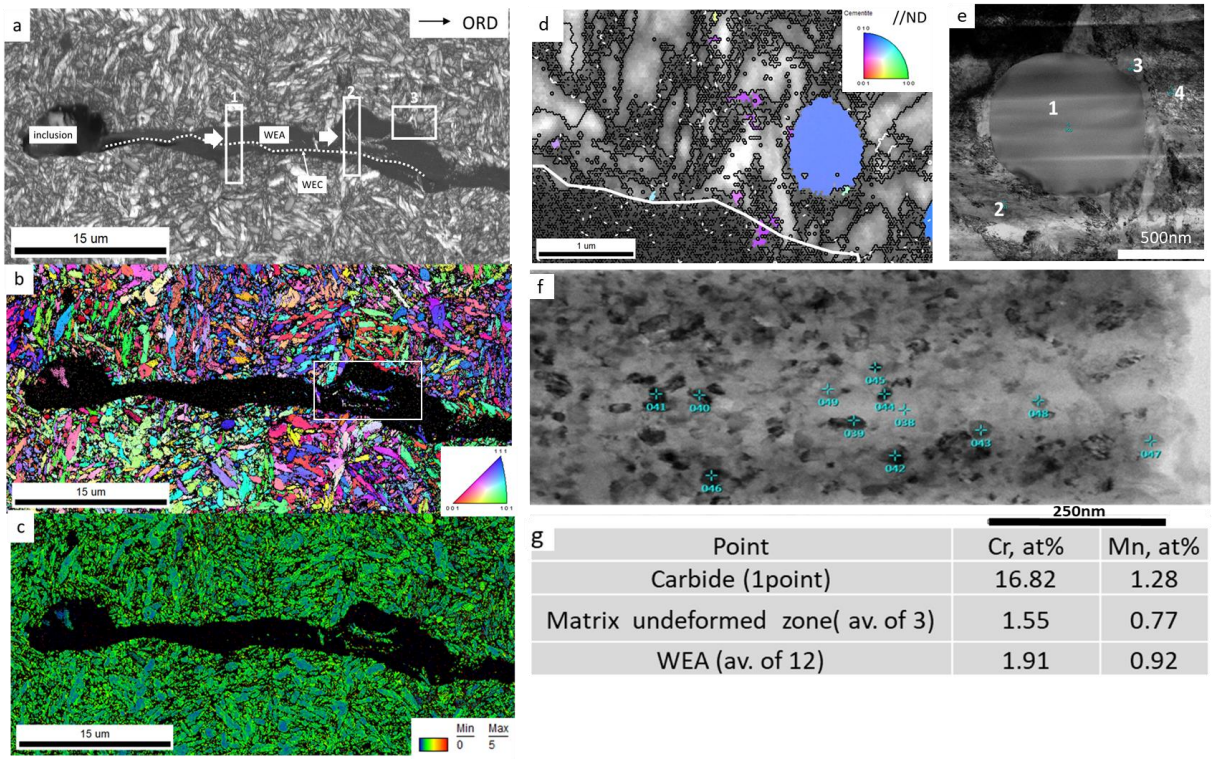


g

| Point | Cr, at% | Mn, at% |
|---|---|---|
| Carbide (1point) | 16.82 | 1.28 |
| Matrix undeformed zone( av. of 3) | 1.55 | 0.77 |
| WEA (av. of 12) | 1.91 | 0.92 |

*Figure 3. EBSD scan of region enclosed in the red square shown in Figure 2, (a) IQ map showing bulk material and WEC within WEA. The white dotted line represents WECs, and the smooth dark area is WEA. The regions enclosed in rectangles labeled 1 and 2 are positions where FIB lamellae are taken, rectangle 3 shows the place of the magnified view in (d); b) ND -Inverse Pole Figure map, white frame shows detectable grains inside WEA; these grains have similar orientations (c) Kernel Average Misorientation map values are calculated using the average misorientation of a given pixel with its third-nearest neighbor (upper limit: 5°). The misorientation determined for the indexed grains is similar to that of the bulk material; (d) A magnified view of the white rectangle 3 in fig. 3a shows a combined IQ and ND-IPF (for carbide map of the close vicinity of the WEA. Black lines are high angle grain boundaries with misorientation >15°, white lines are low angle grain boundaries with a misorientation between 5 and 15°; (e) a bright field TEM image of a single carbide in a matrix of tempered martensite in a not damaged zone close to WEA, with numbers identifying the points for EDS analysis; (f) a bright field TEM image from the WEA with points where the EDS analyses were carried out and (g) averaged results from the EDS analyses.*

The intermediate stage of damage development should not necessarily contain large undissolved carbides, as the “smooth” appearance of the white etching area is observed in the studied zone of the layer. Such carbides were identified only in the close vicinity of the WEA (Fig. 3a, d). If these undissolved carbides are not enough large, they cannot be measured correctly with EBSD. Moreover, the rubbing of the crack surfaces induced severe plastic deformation, but the local stress levels differ across the zone of interest, therefore some of the bcc- grains are still detectable by means of EBSD. Unfortunately, this is not the case for the carbides inside WEA. They are too small (~10-15nm) and cannot be identified via EBSD neither via TKD or ACOM-TEM. Fig. 3 d shows a magnified view from the zone containing the WEA and the undeformed zone. In this figure only the carbides that are larger than 8 pixels and that have a CI>0.2. The fine carbides are identified in the closest vicinity of the WEA but

not detected inside it. The data of TEM /EDS study on FIB lamellae #2 are shown in Fig. 3 e and f. This figure shows the results of analyses of two representative zones of the lamella and only the variations in the Cr, and Mn content were traced, because the C cannot be quantified correctly via EDS and because the Cr and Mn are the slowest diffusing elements in this steel. Hence, it is logical to assume that if these elements are dissolved the C also should be dissolved and hence the carbide will be dissolved. The zone #1 in Fig. 3e contains EDS data from a single carbide from the matrix (single measurement) and from the martensitic matrix (3 measurement, #2, 3 and 4) that are outside the WEA. The second image in Fig. 3f shows a part of the WEA in which clearly the equiaxed small grains can be identified and the points of the EDS measurements are marked with green crosses (12 in total). There are two important conclusions of this observation: *(i)* TEM analysis did not detect individual carbides that can be identified by diffraction; *(ii)* the data from the EDS analyses show that the Cr content of the carbide is ~17at% and in the undeformed matrix it is 1.5at%, whereas the Cr content of the WEA is 1.9at%. Hence, it is logical to deduce that the $M_3C$ carbides ($(Fe, Cr, Mn)_3C$) in the WEA are "dissolved" in the matrix of the nano-crystalline BCC phase which leads to increased Cr content. We realize that this study can be more complete if we would have been able to measure the C distribution and segregation of C in the intermediate zone of the WEA via atom probe tomography as it has been already reported in [18] but unfortunately, we do not have access to such technique.

Figure 4a shows the results of transmission Kikuchi diffraction performed on lamella 1. The left side is the martensitic matrix and the black zone corresponds to WEA (white dash-dot line delineates the transition zone). This zone is non-indexable because the WEA grain size is below the spatial resolution of the EBSD system. The green and red pixels comprising the map correspond to the martensitic matrix, indexed as BCC phase, and carbides indexed as $Fe_3C$ phase, respectively. The KAM value of the matrix is slightly higher than that of the carbides. Figure 4c shows that the average KAM value is 0.5° for cementite and 1° for martensite. This indicates that micro-plastic deformations may have occurred preferentially in the martensitic matrix rather than in the carbides. Similar results are obtained for lamella 2.

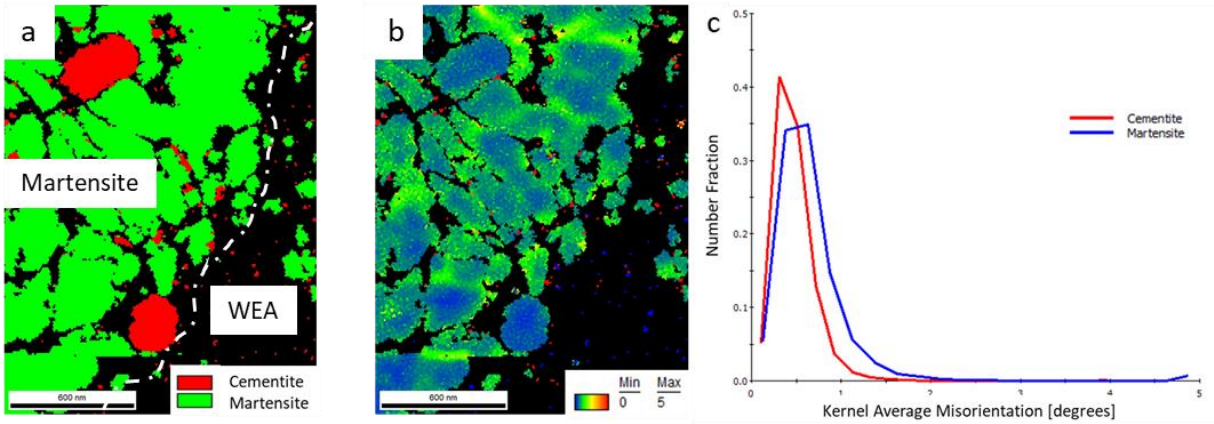


*Figure 4. Transmission Kikuchi diffraction characterization of lamella 1 (corresponding to the region enclosed in the white rectangle shown in Figure 3(a)). (a) The left side of the image corresponds to bulk material and the dark region is the WEA. The transition between these regions is indicated by the white dash-dot line. The grain size is below the detection limit of EBSD and hence the grain structure is unresolved. (b) Kernel average misorientation map of the third-nearest neighbors (upper limit: 5°). The misorientation in the cementite is lower than that in the martensite, suggesting that deformation occurs in the martensite. (c) KAM chart of martensite and cementite.*

As the deformed zone is below the resolution of the TKD system, further TEM analysis is performed to characterize the zone of interest for both lamellas 1 and 2. A bright-field TEM image obtained of lamella 1 (see Figure 5a) reveals uniform grains within the WEA. In contrast, a visible difference in grain sizes is noted for one of the regions in lamella 2, as indicated in Figure 5b, where the white dashed line demarcates zones with different grain sizes.

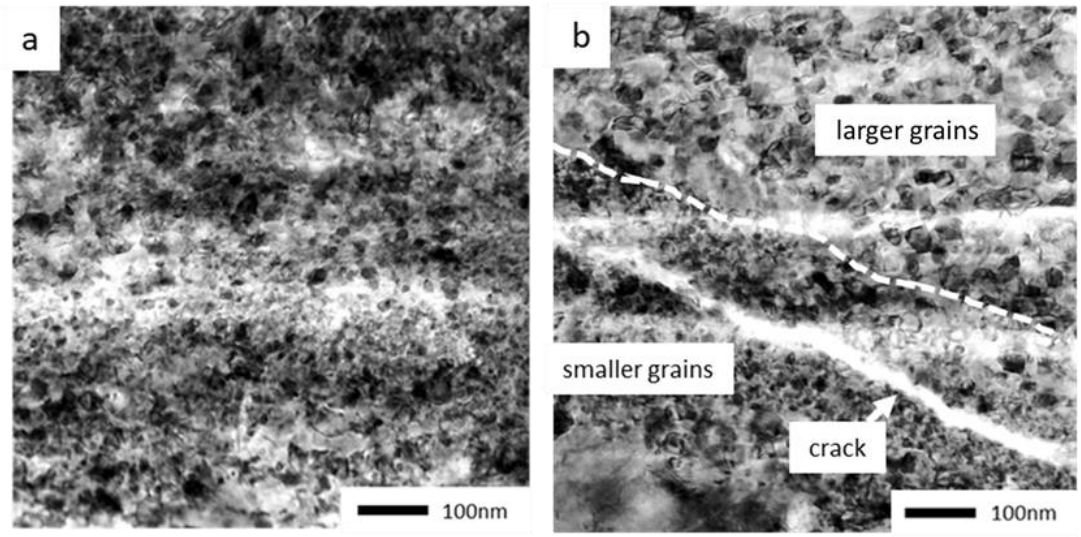


*Figure 5. Bright-field TEM micrograph of WEA lamellas 1 and 2, enclosed in the white rectangles shown in Figure 3a. (a) lamella 1: grain size within the WEA is nearly uniform, (b) lamella 2: difference observed in grain size within the WEA. White dashed line demarcates the regions of different grain sizes. The grains lying in the left bottom side of WEA and vicinal to the crack are smaller than those lying in the top right side.*

### *3.2 Nanostructural characterization of altered zone*

Further characterization of lamella 2 involved ACOM-TEM aimed at evaluating the size and crystallographic orientation of grains inside the WEA (this characterization is impossible with

276 the conventional TKD method). The region of interest is the interface between the martensite
277 matrix and WEA. The IQ map presented in Figure 6a shows that different grayscale gradients
278 occur within martensitic plates. This may have resulted from small internal deviations in each
279 plate, as confirmed by the IPF map (Figure 6b), where variations in the crystallographic
280 orientation are observed. Grains of different sizes occur inside WEA. The IPF map (cf. Figure
281 6b) reveals a very sharp boundary with no transition zone between the small grains inside
282 WEA and the martensitic matrix. Detectable grains inside WEA have different crystallographic
283 orientations. Close examination of the martensitic grains neighboring the fine-grained and
284 possibly deformed zone suggests that these grains started to fragment, thereby forming
285 subgrains inside the martensitic crystals. In Figure 6c, High Angle Grain Boundaries (HAGBs)
286 and Low Angle Grain Boundaries (LAGBs), shown in red and black, respectively, are drawn on
287 the IQ map. The deformed zone is generated mainly from the HAGB, consistent with the
288 results reported elsewhere [32]. Texture analysis may elucidate the deformation mechanism,
289 but lies beyond the scope of the present study. The distribution of the grain size in WEA is
290 shown in Figure 6d. The grain size, represented by the average calculated grain diameter,
291 ranges from a few nm to 50 nm (mode of the distribution: <30 nm).

292

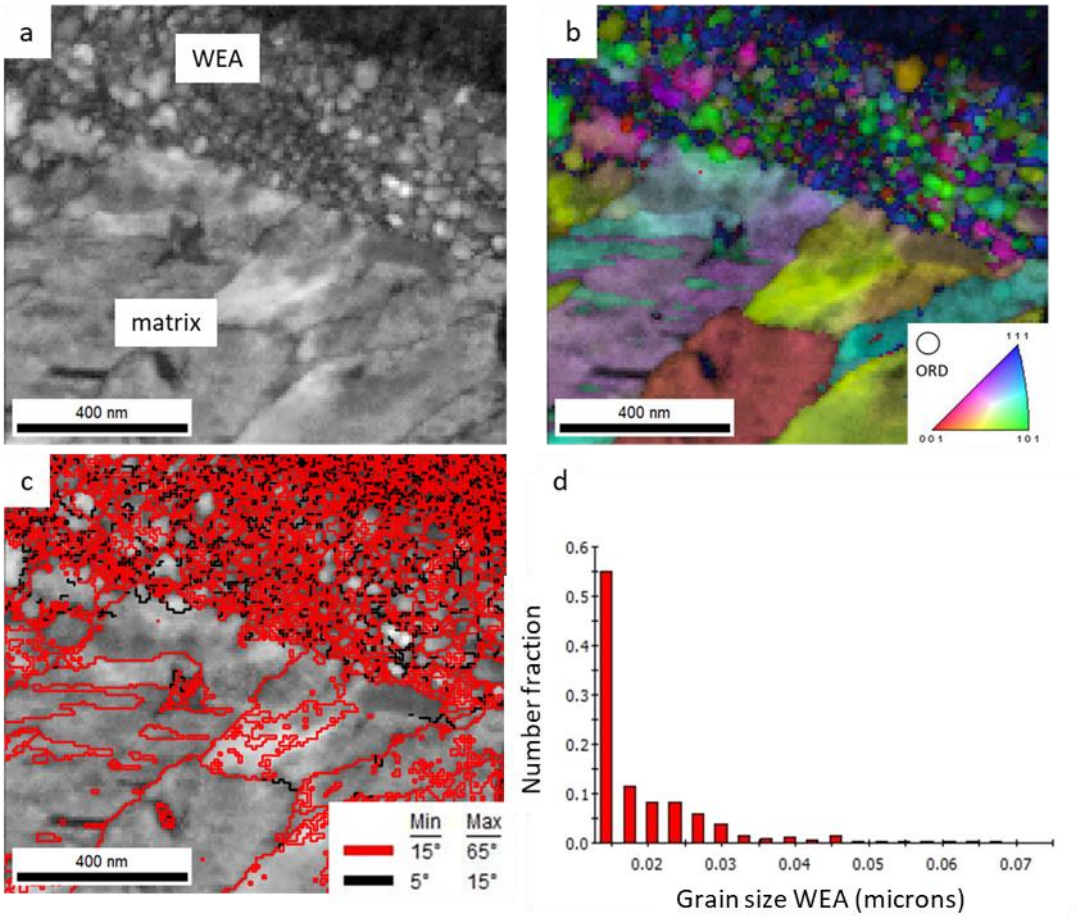


*Figure 6. ACOM TEM of lamella 2, region of interest is the boundary between WEA and the martensitic matrix (a) IQ map with the lower part and the upper part of the image corresponding to the martensitic matrix and WEA, respectively. The grains within WEA are detectable. (b) Inverse Pole Figure Map superimposed on the IQ map. A sharp border between the WEA and the martensitic matrix is observed. The grain orientations vary significantly within the WEA, suggesting that recrystallization has occurred. (c) High Angle Grain Boundaries and Low Angle Grain Boundaries are shown in red and black, respectively. (d) Distribution of grain size within the WEA.*

### *3.3 Verification: The crystallographic orientation of the fragmented grains is similar to that of the vicinal bulk material*

Additional evidence of severe plastic deformation is presented in Figure 7. An EBSD scan performed on the zone of interest captures small spherical and elongated grains within WEA. The IPF map (Figure 7b) reveals that these spherical grains have a similar orientation. This may be attributed to the: *(i)* occurrence of severe plastic deformation where more time (than the processing time) is required for fragmentation of specific grain orientations and hence deformation is incomplete and *(ii)* material transfer from one side of the crack to the other during crack rubbing, as postulated in [13, 28]. The IPF map (Figure 7b) shows that the crystallographic orientation of these grains is similar to that of the vicinal non-deformed martensitic matrix. Kernel Average Misorientation analysis revealed that the misorientation within small spherical grains is the same as that of the bulk material, suggesting that the

fragmented grains are unrecrystallized. Figure 8 (a) shows the enlarged area from Figure 7b, (b) the Color code key for the IPF map. (c) are ND-IPF texture representations of the marked zones from 1 to 4 in Fig. 8(a). Zones 1 to 3 represents BCC grains inside the WEA. The orientation of these grains is similar to the crystallographic orientation of martensite. This is shown in ND-IPF charts which are selected as follows. Charts 1 to 3 is a deformed zone, whereas chart 4 is a general texture from non-deformed martensite. Comparatively, all the elements from the non-deformed zone can be recognized in zones 1 to 3. However, comparing intensities is not correct, only texture components, because the number of points within zones is different.

## 4. Discussion

The obtained results suggest that the captured damage corresponds to the intermediate stage of development where severe plastic deformation occurred partially, but without recrystallization. As shown in [13, 28], the crack is initiated from a defect in the material and this initiation is followed by severe plastic deformation. The mechanical rubbing of the crack surfaces is insufficient for inducing recrystallization of the entire WEA volume, and hence large grains remain unchanged within WEA.

With the provided evidence, the following chronology of events is proposed for the creation of a WEA and WECs in bearing steel. One of the difficulties associated with the characterization of the WEC phenomenon is that most bearings are studied post-mortem. Capturing the intermediate stages of the damage development process is therefore quite difficult. Characterization of the field bearing revealed that WEA is unequally distributed on the sides of the crack and its location differs between the lower and upper parts. The lower and upper parts are designated with respect to the over-rolling load. The WEC appears interrupted (Figure 2), owing possibly to the two-dimensional nature of observation. Moreover, the development of WEA is especially interesting, with an irregular shape occurring in specific regions, and a few micrometers from these regions WEA points downward and changes plane. Furthermore, IPF maps (Figure 3) show that WEA does not follow prior austenite grain boundaries. This suggests that cracking may have resulted from factors other than PAGBs serving as nucleation and propagation sites for cracks.

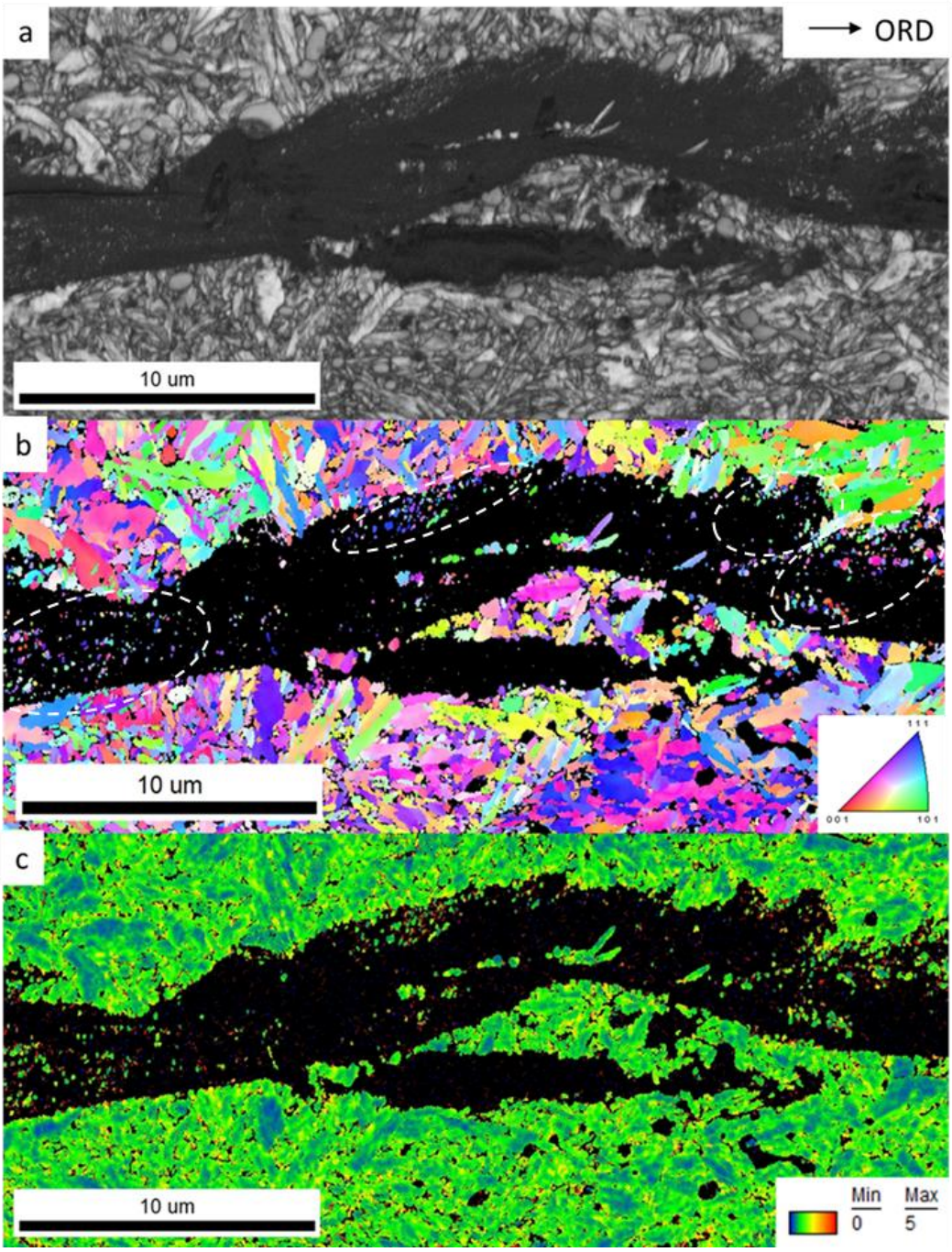


*Figure 7. (a) IQ map of region containing WEC and WEA, (b) IPF map showing small spherical grains inside WEA (white dashed ovals) with similar orientation to that of the bulk material, and (c) KAM map values are calculated using the average misorientation of a given pixel with its third neighbor (upper limit: 5°). The misorientation of detectable grains inside WEA is similar to that of the bulk material.*

Grabulov [13] reported that cracks move a few nm upon each cycle, leaving behind WEA. However, the weakest link in the material and the crack propagation path remain unidentified. Future work on this topic would be necessary for drawing additional conclusions on crack propagation.

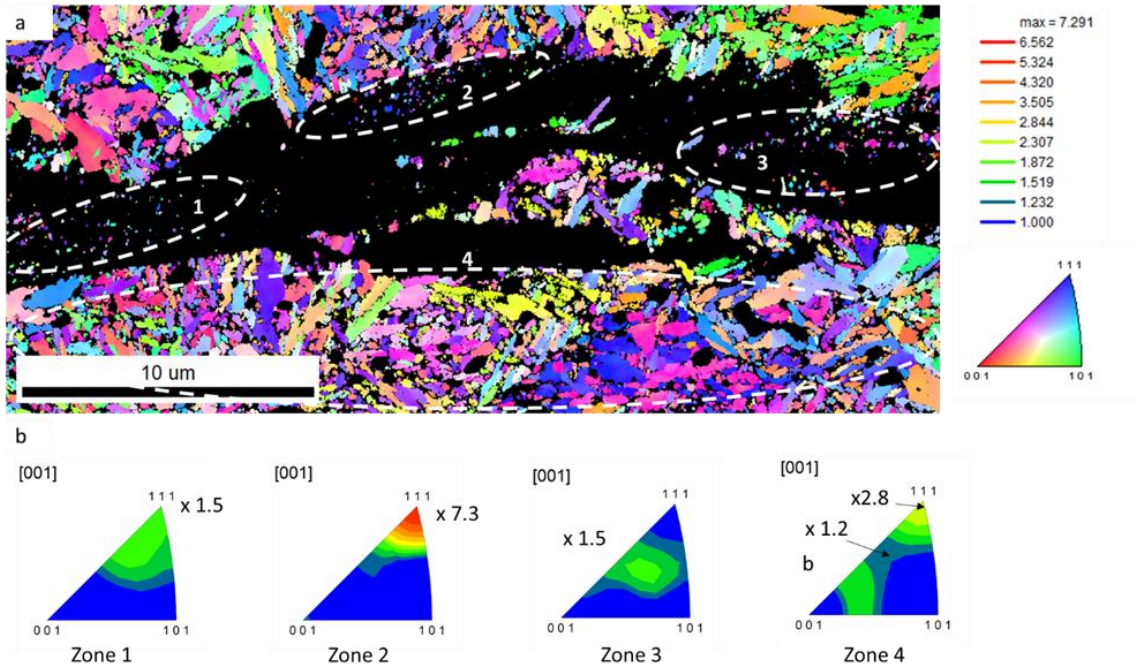


*Figure 8. (a) A color coded ND-IPF map of the BCC phase in WEA and its close vicinity. (b) Color code key for the IPF map. (c) are ND-IPF texture representations of the marked zones from 1 to 4 in Fig. 8(a). All textures are calculated with respect to the maximum of 7x mrd (multiples of random density) using a Gaussian half width of 5° and series rank of L=16.*

The EBSD scan on a region of interest reveals needle-like martensitic grains embedded within WEA (Figure 3). Although this phenomenon is observed by other authors [ref, 22, 30] a direct comparison with the previously reported data is difficult due to significant differences in the experimental conditions-real loading conditions vs: laboratory test or hydrogen charged bearings vs atmospheric condition etc. Further analysis of TEM lamellae from the same region revealed that lamella 1 has a uniform grain size within WEA, while lamella 2 has a bimodal grain size distribution. TKD measurements performed on lamella 1 shows that deformation occurs in the martensitic matrix rather than in carbides. ACOM-TEM of lamella 2 revealed a very sharp interface between two zones. The crystallographic orientation of the grains inside WEA varies significantly, consistent with the occurrence of recrystallization. The grain size of WEA ranges from 10 nm to 50 nm. An EBSD scan of the same zone reveals (Figure 7) clusters of small spherical grains inside WEA. The orientation of each cluster (enclosed in white dotted oval) is similar to the orientation of the vicinal undeformed martensitic matrix. This may have resulted from an incomplete severe plastic deformation process or material transfer, fatigue cracks generated by non-metallic inclusions, SPD resulting from crack face rubbing, and dynamic recrystallization controlling the grain size of WEA. Therefore, in this specific case, the intermediate stage of damage is captured in the case of severe plastic deformation, but

recrystallization is prevented, owing to insufficient time/rolling contact cycles for the process to occur.

Microstructural observations via ESBD, TEM, and ACOM-TEM suggest that the nanocrystalline structure is generated by severe plastic deformation. Hence, through TEM micrographs of both samples, a correlation between the bimodal grain size within WEA and other factors is derived. These findings are consistent with APT [33] measurements of the different sections comprising WEA and large-grained WEAs have low carbon contents. Moreover, a correlation between the grain size and source of carbon (decomposition of carbides) was found, i.e., the highest carbon content of the smallest grains (size: <10 nm) was 9.5 at% in ferrite. In contrast, no grain-size correlation was observed for the chromium content. The findings suggest that carbon leads to grain size stabilization in WEA through extensive grain boundary segregation[33] .

As previously mentioned, in both cases, carbides in the vicinity of WEA undergo no plastic deformation, and no traces of dissolution are found. This indicates that severe plastic deformation has occurred.

## 5. Conclusions

In this study, a field bearing is characterized by employing SEM, EBSD, TKD, TEM, and ACOM TEM. The objective is to understand the damage mechanism of the bearing. Hence, short WECs (~20 µm) with incomplete damage development are investigated. In this investigation, the intermediate stage of damage development is captured and WEC/WEA phenomena are elucidated. The main findings of the study are summarized as follows:

- WEA consists of small grains with sizes lower than 30 nm. The crystallographic orientation of the grains in the deformed zone suggests that recrystallization has occurred.
- TEM measurements revealed that WEA consists of zones with different grain sizes.
- EBSD and TKD measurements revealed that micro-plastic deformation occurs in the martensitic matrix rather than in the carbides.

- Carbides in the vicinity of the WEA remain undissolved and undeformed, suggesting that SPD has occurred.
- The crystallographic orientation of detectable grains in the deformed zone is similar to that of the vicinal bulk material.
- A very sharp interface between the martensitic matrix and the WEA, with no apparent transition zone, is detected by all observation techniques.

The findings strongly suggest that the process of WEA formation in the bearing steel is controlled by severe plastic deformation and recrystallization of martensite into nanocrystalline ferrite.

**Acknowledgements:** The authors gratefully acknowledge the financial support provided by the MaDurOS program from VLAIO (Flemish Agency for Innovation and Entrepreneurship) and SIM (Strategic Initiative Materials) through project SBO MaSiWEC (HBC.2017.0606).

## 6. References

[1] M. d. G. Carvalho, "EU energy and climate change strategy," *Energy,* vol. 40, no. 1, pp. 19–22, 2012.

[2] K. Marvel, B. Kravitz, B. Kaldeira, "Geophysical limits to global wind power," *Nature Climate Change,* no. 3, pp. 118–121, 2012.

[3] "Wind in power 2017," Windeurope, Brussels, 2018.

[4] N. Akbari, D. Jones, R. Treloar, "A cross-European efficiency assessment of offshore wind farms: A DEA approach," *Renewable Energy,* vol. 151, pp. 1186–1195, 2020.

[5] "Wind Europe," 29 March 2019. [Online]. Available: https://windeurope.org/policy/topics/economics/.

[6] M. D. Reder, E. Gonzales, J. J. Melero, "Wind turbine failures - Tackling current problems in failure data analysis," *Journal of Physics: Conference Series,* vol. 753, no. 7, 2016.

[7] M.-H. Evans, A. D. Richardson, L. Wang, R. J. K. Wood, W. B. Anderson, "Confirming subsurface initiation at non-metallic inclusions as one mechanism for white etching crack (WEC) formation," *Tribology International,* vol. 75, pp. 87–97, 2014.

[8] J. Lai, K. Stadler, "Investigation on the mechanisms of white etching crack (WEC) formation in rolling contact fatigue and identification of a root cause for bearing premature failure," *Wear,*vols. 364-365, pp. 244–256, 2016.

[9] A. Reid, M. Marshall, I. Martinez, S. Moorby, T. Connolley, M. Mostafavi, S. Kabra, "Measurement of strain evolution in overloaded roller bearings using time-of-flight neutron diffraction," *Materials & Design,* vol. 190, 2020.

[10] K. Sreeraj, P. Ramkumar, "Replication of white etching area evolution using novel modified dynamic load pin-on-disc tribometer on bearing steel," *Tribology International,* vol. 126, pp. 336–343, 2018.

[11] K. Iyas, D. Kurten, R. Raga, N. Winzer, A. Kailer, "Modeling hydrogen diffusion in a tribological scenario: A failure analysis of a thrust bearing," *Wear,* Vols. 438–439, 2019.

[12] F. Gutiérrez Guzmán, M. Oezel, G. Jacobs, G. Burghardt, C. Broeckmann, T. Janitzky, "Reproduction of white etching cracks under rolling contact loading on thrust bearing and two-disc test rigs," *Wear,* Vols. 390–391, pp. 23–32, 2017.

[13] A. Grabulov, "Ph.D. Thesis, Fundamentals of Rolling Contact Fatigue," TU Delft, 2010.

[14] A. Warhadpande, F. Sadeghi, R. D. Evans, "Microstructural alterations in bearing steels under rolling contact fatigue part 1—Historical overview," *Tribology Transactions,* vol. 56, pp. 349-358, 2013.

[15] S. M. Moghaddam, F. Sadeghi, "A review of microstructural alterations around nonmetallic inclusions in bearing steel during rolling contact fatigue," *Tribology Transactions,* vol. 59, pp. 1142–1156, 2016.

[16] A. T. W. Barrow, J.-H. Kang, P. E. J.Rivera-Díaz-del-Castillo, "The $\epsilon \rightarrow \eta \rightarrow \theta$ transition in 100Cr6 and its effect on mechanical properties," *Acta Materialia,* vol. 60, no. 6–7, pp. 2805–2815, 2012.

[17] H. Bhadeshia, "Steels for bearings," *Progress in Materials Science,* vol. 57, pp. 268–435, 2012.

[18] Y. J. Li, M. Herbig, S. Goto, D. Raabe, "Atomic scale characterization of white etching area and its adjacent matrix in a martensitic 100Cr6 bearing steel," *Materials Characterization,* vol. 123, pp. 349–353, 2017.

[19] J.-H. Kang, B. Hosseinkhani, C. A. Williams, M. P. Moody, P. A. J. Bagot, P. E. J. Rivera-Dı´az-del-Castillo, "Solute redistribution in the nanocrystalline structure formed in bearing steels," *Scripta Materialia,* vol. 69, pp. 630–633, 2013.

[20] H. K. Danielsen, F. Gutiérrez Guzmán, K. V. Dahl, Y. J. Li, J. Wu, G. Jacobs, G. Burghardt, S. Fæster, H. Alimadadi, S. Goto, D. Raabe, R. Petrov, "Multiscale characterization of White Etching Cracks (WEC) in a 100Cr6 bearing from a thrust bearing test rig," *Wear,* vols. 370-371, pp. 73–82, 2017.

[21] M.-H. Evans, J. C. Walker, C. Ma, L. Wang, R. J. K. Wood, "A FIB/TEM study of butterfly crack formation and white etching area (WEA) microstructural changes under rolling contact fatigue in 100Cr6 bearing steel," *Materials Science and Engineering A,* vol. 570, pp. 127–134, 2013.

[22] A. Grabulov, R. Petrov, H. W. Zandbergen, "EBSD investigation of the crack initiation and TEM/FIB analyses," *International Journal of Fatigue,* vol. 32, pp. 576–583, 2010.

[23] V. Smelova, A. Schwedt, L. Wang, W. Holweger, J. Mayer, "Microstructural changes in White Etching Cracks (WECs) and their relationship with those in Dark Etching Region (DER) and White Etching Bands (WEBs) due to Rolling Contact Fatigue (RCF)," *International Journal of Fatigue,* vol. 100, pp. 14–158, 2017.

[24] M. E. Curd, T. L. Burnett, J. Fellowes, P. Yan, P. J. Withers, "Redistribution of carbon caused by butterfly defects in bearing steels," *Acta Materialia,* vol. 183, pp. 390–397, 2020.

[25] M. Paladugu, R. Scott Hyde, "Material composition and heat treatment related influences in resisting rolling contact fatigue under WEC damage conditions," *International Journal of Fatigue,* vol. 134, 2020.

[26] M. E. Curd, T. L. Burnett, J. Fellowes, J. Donoghue, P. Yan, "The heterogeneous distribution of white etching matter (WEM) around subsurface cracks in bearing steels," *Acta Materialia,* vol. 174, pp. 300–309, 2019.

[27] A. M. Diederichs, A. Schwedt, J. Mayer, T. Dreifert, "Electron microscopy analysis of structural changes within white etching areas," *Materials Science and Technology,* vol. 32, pp. 1683–1693, 2016.

[28] L. Morsdorf, D. Mayweg, Y. Li, A. Diederichs, D. Raabe, M. Herbig, "Moving cracks form white etching areas during rolling contact fatigue," *Materials Science & Engineering A,* vol. 771, 2020.

[29] H. Fu, P. E. J. Rivera-Díaz-del-Castillo, "A unified theory for microstructural alterations in bearing steels under," *Acta Materialia,* vol. 155, pp. 43–55, 2018.

[30] M. Oezel, A. Schwedt, T. Janitzky, R. Kelley, C. Bouchet-Marquis, L. Pullan, C. Broeckmann, J. Mayer, "Formation of white etching areas in SAE 52100 bearing steel under rolling fatigue - Influence of diffusible hydrogen," *Wear,* Vols. 414–415, pp. 352–365, 2018.

[31] E. F. Rauch, L. Dupuy, "Rapid spot diffraction patterns identification through template matching," *Archives of Metallurgy and Materials,* vol. 50, no. 1, pp. 87–99, 2005.

[32] C. G. He, H. H. Ding, L. B. Shi, J. Guo, E. Meli, Q. Y. Liu, A. Rindi, Z. R. Zhou, W. J. Wang, "On the microstructure evolution and nanocrystalline formation of pearlitic wheel material in a rolling-sliding contact," *Materials Characterization,* vol. 164, 2020.

[33] D. Mayweg, L. Morsdorf, Y. Li, M. Herbig, "Correlation between grain size and carbon content in white etching," *Acta Materialia,* vol. 215, no. 117048, 2021.

[34] M.-H. Evans, "White structure flaking (WSF) in wind turbine gearbox bearings: effects of 'butterflies' and white etching cracks (WECs)," *Materials Science and Technology,* no. 28, pp. 3–22, 2012.

423

424